

1 Revision_1

2 Cation distribution and valence in synthetic Al-Mn-O and Fe-Mn-O
3 spinels under varying fO_2 conditions.

4 T. N. Stokes¹, G. D. Bromiley, G. D. Gatta², N. Rotiroti², N. J. Potts¹ and K. Saunders¹

5 ¹School of GeoSciences, University of Edinburgh, King's Buildings, Edinburgh, EH9 3FE, UK

6 ²Dipartimento di Scienze della Terra, Università degli Studi di Milano, Via Botticelli 23, I-20133

7 Milano, Italy

8

9 ABSTRACT

10 The spinel group minerals, found in a range of igneous rocks, are resistant to weathering and can
11 incorporate several multivalent elements, meaning they have the potential to provide insight into
12 redox conditions of parental magmas. Naturally occurring spinel can contain varying quantities of
13 Mn, an element which occurs terrestrially and extraterrestrially as Mn²⁺, Mn³⁺, Mn⁴⁺ and Mn⁵⁺.
14 However, a lack of information on the effects of oxygen fugacity (fO_2) on: (1) Mn valence state and
15 cation distribution, and (2) on spinel-melt partitioning means that the potential for a Mn-in-spinel
16 oxy-barometer remains largely untested. Here, we use electron probe microanalysis, micro-focus X-
17 ray Absorption Near Edge Structure (XANES) spectroscopy and single crystal X-ray diffraction (SC-
18 XRD) to investigate cation distribution and valence state in spinels in the Al-Mn-O and Fe-Mn-O
19 systems synthesized at ambient pressure under varying fO_2 conditions. In contrast to previous
20 studies, we find that the spectral resolution of the Mn K edge XANES spectra is insufficient to
21 provide quantitative data on Mn valence state and site occupancy, although it does verify that Mn is
22 incorporated as both Mn²⁺ and Mn³⁺, distributed over tetrahedral and octahedral sites. Combination

23 of data from XANES and SC-XRD refinements can, however, be used to model Mn, Al and Fe valence
24 and site occupancy. Mn-Fe spinels have the potential to record fO_2 conditions in parental melts due
25 to changes to the octahedral site under more reducing conditions. However, decoupling the effects
26 of temperature and oxygen fugacity on the ${}^{\text{T}}\text{Fe}^{3+}\text{-}^{\text{T}}\text{Mn}^{2+}$ exchange in the Mn-Fe spinels remains
27 challenging. In contrast, little variation is noted in Mn-Al spinels as a function of fO_2 , implying that
28 crystal chemistry and cation site geometry may significantly influence cation distribution, and by
29 inference, crystal-melt partitioning, in spinel group minerals.

30 Keywords: spinel, manganese, XANES, oxygen fugacity, jacobsite, galaxite.

31

32 1. Introduction

33 Oxide minerals of the spinel group (from here on referred to as spinels), alongside being important
34 constituents of the uppermost mantle, are common accessory minerals in both igneous and
35 metamorphic rocks, and commonly occur as detrital grains in sedimentary deposits. Furthermore,
36 spinels are found in a wide range of extra-terrestrial samples with their ubiquity suggesting an early
37 role in the formation of the solar system (Roeder 1994). Spinel group minerals are useful
38 petrogenetic indicators in terrestrial magmas because they form complex solid solutions which
39 crystallize in a wide range of magmatic compositions. Spinel can be found as both early and late
40 crystallising phases during magma fractionation, and are often the first phase to form (Barnes and
41 Roeder 2001). When compared to other high temperature igneous minerals such as olivine, spinels
42 are fairly resistant to chemical and physical alteration (Cookenboo et al. 1997). Therefore, detrital
43 spinel found in early sedimentary deposits could record conditions (*e.g.* temperature, redox
44 conditions, and pressure) prevalent in early Earth's history.

45

46 Spinel s tend to have high partition coefficients for trace elements in magmatic systems.
47 Consequently, crystallisation of a spinel phase strongly influences the budgets of trace elements. The
48 partitioning of elements between spinels and silicate melts is strongly affected by temperature (T),
49 oxygen fugacity (fO_2) and spinel composition (Righter et al. 2006), and may also be affected by
50 pressure (P). Spinel geochemistry can, therefore, be used as an important tool in determining
51 fractionation trends of magmas and the trace element budget of primary basaltic magmas (Wijbrans
52 et al. 2015), which gives insight into the source region of these melts in the mantle. The potential of
53 spinels to determine fO_2 is important for further understanding magmatic differentiation, mineral
54 assemblages and elemental partitioning (Sato 1978). As well as controlling the chemistry of magmas,
55 spinel composition is sensitive to changes in the chemistry of the surrounding magma because of
56 several substituting cations which can subtly change according to the physico-chemical conditions of
57 the parental melt (Arai 1992).

58

59 The complex chemistry of spinels in igneous systems is due to the extensive solid solutions and the
60 extent of cation disorder across different crystallographic sites. Diversity in natural spinels also arises
61 from the valence of the cations found in either the tetrahedral or octahedral sites. Divalent, trivalent,
62 and tetravalent cations can all be accommodated into the spinel structure, and many transitional
63 elements can be present in varying amounts of multiple valences. The general formula of spinels is
64 typically expressed as AB_2O_4 , where A and B are different cations. Common cations include Mg, Fe,
65 Al, Zn, Mn, Cr, Ga, Ti, and Si. Spinel s are also an important mineral group for industrial and
66 technological applications due to their extraordinary catalytic, electrical, optical, and magnetic
67 properties (Carta et al. 2013), which arises from their ability to incorporate many transitional
68 elements into their structure (*e.g.* Fe, Mo, Zn, Ti, Cr, Mn and V).

69

70 Galaxite (MnAl_2O_4) and jacobsite (MnFe_2O_4) are two Mn spinel end members. In nature, galaxite
 71 often forms in carbonate-rich silica under-saturated metamorphosed Mn deposits (Anthony et al.
 72 1997). Jacobsite generally forms as a primary mineral or alteration product in similar
 73 metamorphosed Mn deposits (Anthony et al. 1997). The structure of jacobsite, galaxite, and other
 74 oxide minerals with a spinel structure, consists of oxygen atoms arranged in a cubic close packed
 75 (ccp) structure, with cations filling 1/8 of the tetrahedral (T) and 1/2 of the octahedral (M) sites. An
 76 excess of metal cations will occupy normally vacant interstitial sites (Fleet 1981; Henderson et al.
 77 2016). The typical space group symmetry of spinels is $Fd\bar{3}m$. In an ideal '2-3 spinel' structure,
 78 divalent cations are housed on the T site, whilst trivalent cations are present on the M site. Spinel
 79 group minerals typically display variable degrees of disorder of A and B cations across the T and M
 80 sites (Redfern et al. 1999). The amount of cation disorder can be described using the inversion
 81 parameter i , which is defined by the equation:

$$83 \quad A_{1-i}B_i \left(A_i B_{1-\frac{i}{2}} \right)_2 O_4 \quad [1]$$

84 When $i = 0$, a '2-3' spinel is described as completely normal ($T^A M^B O_4$), whereas $i = 1$ describes an
 85 'inverse' configuration ($T^B M^A O_4$), and an inversion parameter of 0.67 indicates a completely
 86 disordered spinel. In a completely normal spinel, A ions fully occupy the T sites, whilst the M site is
 87 filled by B cations. Inverse spinels have half of the B and all the A cations on the M site, whilst the
 88 other B cations fully occupy the T sites. At high temperatures, i tends toward complete disorder for
 89 all compositions. '4-2' spinels are rarer than '2-3' spinels and have a tetravalent A cation, and
 90 divalent B cation (Biagioni and Pasero 2014).

91

92 Jacobsite is a nominally 'normal' Fe^{3+} - Mn^{2+} 2-3 spinel. However, the actual assignment of cation
 93 oxidation states is difficult due to (1) the multivalence characteristic of both Mn and Fe, (2) the

94 equilibrium $\text{Mn}^{2+} + \text{Fe}^{3+} \rightleftharpoons \text{Mn}^{3+} + \text{Fe}^{2+}$, (3) electron hopping between cation sites (Biagioni and
95 Pasero 2014), and (4) the similar atomic number of these elements. Fe-Mn spinels are of particular
96 interest to industry because they provide improved performance catalysts in Fischer Tropsch
97 synthesis (Herranz et al. 2006), are used as negative temperature coefficient (NTC) thermistors
98 (Battault et al. 1995), act as contrasting agents in MRI imaging (Lu et al. 2009), and as hyperthermia
99 agents in cancer treatment (Kim et al. 2009). Galaxite is also a 'normal' spinel, although in this case
100 assignment of Mn oxidation state is simpler due to the significant difference in atomic number
101 between Al and Mn, as well as the single valence state of Al within spinels.

102

103 Recent work on spinel group minerals within Earth sciences has focussed on the development of
104 calibrated thermometers, barometers, and oxygen barometers based on the partitioning of redox
105 sensitive trace elements between spinel and melts, for use when conventional methods cannot be
106 performed (*e.g.* Canil 1999; Righter et al. 2006; Burger et al. 2016; Arató and Audétat 2017).
107 Manganese is a redox sensitive element which readily substitutes into both the tetrahedral and
108 octahedral crystallographic sites in the spinel structure, and can be present either as Mn^{2+} , Mn^{3+}
109 and/or Mn^{4+} . Mn also can be present in multiple oxidation states on the same or different sites.
110 However, little is known on the behaviour of Mn in the spinel structure as a function of P, T and fO_2 ,
111 or the extent to which Mn speciation and partitioning into spinels can be used to probe fO_2
112 conditions in magmas.

113

114 Measuring valence states can be challenging in the simple end member spinels, and is further
115 complicated in the solid solutions. The arrangement of cations in the spinel structure is often
116 investigated using X-ray diffraction (XRD) and neutron diffraction (ND) data. However, this data can
117 be ambiguous in spinels which contain cations with similar scattering properties, and is further
118 complicated by the coupled effects of changes in valence state and ordering. Determining the

119 oxidation state of cations on the *T* and *M* sites is also very difficult as most techniques cannot
120 differentiate the valence state of cations. ⁵⁷Fe Mössbauer spectra provides important data for the
121 valence, coordination, and ordering of Fe cations but fails to distinguish Fe³⁺ and Fe²⁺ above the
122 Verwey transition temperature (Henderson et al. 2016). Furthermore, Mössbauer cannot always
123 distinguish Fe³⁺ site occupation between *M* and *T* sites (Zhang et al. 1998), and is only applicable for
124 cations with a Mössbauer spectrum. X-ray absorption near edge structure (XANES) spectroscopy is a
125 method which is becoming increasingly common in determining oxidation state and coordination
126 state in geological materials. Unlike electron energy loss spectroscopy (EELS), XANES is a non-
127 destructive technique which can obtain spectra from samples mounted for optical and electron
128 microscopy. As spinel is an isotropic mineral, XANES spectra can be recorded from any grain without
129 having to account for the effects of crystallographic orientation (Berry et al. 2010).

130

131 Here, XANES K-edge data are used to provide averaged site information, which is combined with
132 single crystal X-ray diffraction (SC-XRD) structural refinements and compositional data from electron
133 microprobe analyses (EMPA) to provide an estimate for cation coordination and valence in synthetic
134 **jacobsite- and galaxite-like spinels (from here on, just referred to jacobsite and galaxite)**. This
135 multidisciplinary approach is used to estimate the cation distribution and oxidation state for Al, Mn
136 and Fe across the *T* and *M* sites, using previously published cation site preferences. Varying *f*O₂
137 conditions during synthesis are used to determine the effect of redox on either the amount, valence,
138 or distribution of Al, Mn, and Fe in jacobsite and galaxite to determine the potential of an oxy-
139 geobarometer based on Mn-in-spinel.

140

141 **2. Mineral synthesis**

142 Single crystals of jacobsite and galaxite were synthesized using a similar flux growth method to that
143 of Andreatti (1999). Starting mixtures were prepared from stoichiometric proportions of analytical
144 grade powders (MnO_2 , Al_2O_3 , and Fe_2O_3) and mixed with anhydrous borax ($\text{Na}_2\text{B}_4\text{O}_7$), the flux
145 compound. The starting material was weighed and homogenized by grinding under acetone in an
146 agate mortar before being placed in a Pt/Au(5%) crucible. This type of crucible was selected due to
147 its low wettability and high resistance to chemical attack at high temperatures under reducing
148 conditions. Experimental runs were performed using a platinum wound vertical tube gas-mixing
149 furnace with Bronkhorst mass flow controllers. Oxide and flux mixes were heated to 1200 °C for 1
150 hour before cooling at 12.5 °C/hr to the final run temperature of 900 °C, then held for 24 hours,
151 before being rapidly quenched. Each experiment (except for Ga60, which was quenched by quickly
152 raising the charge out of the hotspot) was drop quenched into water upon completion of the run. A
153 mixture of CO_2/H_2 gas was used to control the oxygen fugacity conditions during synthesis (Deines et
154 al. 1974), with $f\text{O}_2$ values confirmed using an Australian Oxytrol Systems solid zirconia electrolyte
155 oxygen sensor (SIRO2 sensor). Runs JcAC and GaAC were both run with the furnace open to air (Log
156 $f\text{O}_2$ (air) = -0.68 for all temperatures, if we assume it is behaving as an ideal gas). Runs suffixed by 93,
157 90, and 60 indicate the % CO_2 used in the gas mix, and equate to $\log f\text{O}_2 = -13.8, -14.2, \text{ and } -15.8,$
158 respectively, at 900°C. Recovered spinels were mounted in epoxy, ground, and polished using
159 standard diamond solutions for XANES and EMPA analysis. Individual crystals of each sample were
160 selected for high-quality XRD analysis, and examined optically to ensure absence of twinning and
161 inclusions.

162

163 **3. Analytical methods**

164 **3.1 EMPA**

165 Compositions were determined with a Cameca SX-100 electron microprobe, using an accelerating
166 voltage of 15KeV, a 20 nA beam current with a 2 μm effective beam diameter. Primary standards and

167 analysing crystals were as follows: Al (Spinel BL8, TAP, 593.6 cps/nA), Mn (Tephroite, LLIF, 247.4
168 cps/nA), O (Tephroite, PCO, 46.4 cps/nA), and Fe (Fayalite, LLIF, 300.4 cps/nA). K α lines were used
169 for all analyses. Sample Ga60 was measured using a JEOL JXA8530F Hyperprobe, at the University of
170 Bristol. Data for this sample was collected with an accelerating voltage of 15keV, a 10 nA beam
171 current, and a 1 μ m beam diameter. Primary standards and analysing crystals were as follows: Al (B4
172 Spinel, TAP), Mn (Mn metal, LLIF) and Fe (Fayalite, LLIF). Transects of larger crystals indicate crystals
173 are chemically homogenous, unzoned in Fe/Mn/Al/O content. However, for some samples, up to 1.2
174 wt % standard deviations may suggest some minor compositional variation between crystals from
175 the same run.

176

177 *3.2 X-ray absorption spectroscopy*

178 Mn K-edge and Fe K-edge XANES spectra were collected on beamline I18 at the Diamond Light
179 Source (DLS), Harwell, UK. These spectra were acquired in fluorescence geometry, with samples
180 angled at 80° to the incident beam. A Si(111) double crystal monochromator was used to finely tune
181 the energy of the beam, which was focused on the sample with a spot size of 6 μ m. Scans were
182 measured over an energy range of 6400–6570 eV for the Mn K-edge and 7000–7320 eV for the Fe K-
183 edge. Step size for Mn XANES scans across the pre-edge peak and main edge region was 0.25 eV.
184 Step size for Fe XANES data was 0.25 eV over the pre-edge peak and 0.3 eV across the edge region.
185 Following data collection, scans were imported into the ATHENA program (Ravel and Newville 2005)
186 where spectra were deglitched, aligned, merged, and normalized using standard in-built routines.
187 The Fluo algorithm (Haskel 1999) was applied to correct for self-absorption. A reference foil of Mn
188 and Fe was used for energy calibration of the monochromator, which was applied to all spectra. The
189 Fe K-edge calibration was set to the first inflection point of the reference foil, set at 7112 eV, and
190 corrected to 7110.75 eV (Kraft et al. 1996) for easy comparison with other work. The Mn K-edge
191 calibration was set to the first inflection point in Mn foil, set at 6539 eV and corrected to 6537.67 eV

192 (Kraft et al. 1996). The AUTOBK algorithm was used to model and remove the background using a
193 spline fit procedure. Following normalisation data were then exported to the Fityk software (Wojdyr
194 2010) where a convex hull spline fit was used to subtract the background from pre-edge peaks, prior
195 to the fitting of Gaussian peaks.

196

197 3.3 Single crystal XRD

198 Crystals of galaxite and jacobsite, observably free of defects and untwinned under a polarized
199 transmitting-light microscope, were selected for single-crystal X-ray diffraction experiments at the
200 Dipartimento Scienze della Terra, Università degli Studi di Milano. A preliminary test on the crystal
201 quality was performed using a KUMA KM4 four-circle diffractometer, equipped with a point-detector
202 and a monochromatized MoK α radiation, by the analysis of the profile of the diffraction peaks;
203 samples with poorer observed crystallinity were discounted. Intensity data were then collected using
204 an Oxford Diffraction Xcalibur diffractometer, equipped with a CCD detector and operating at 50 kV
205 and 40 mA, with monochromatized MoK α radiation. A combination of ω scans, with 1° step and 10 s
206 exposure time per frame, was chosen to maximize the redundancy and data coverage. For all the
207 data collections, the reflection conditions agreed with the space group $Fd\bar{3}m$, as expected for
208 galaxite and jacobsite. Intensity data were then integrated and corrected for Lorentz-polarization
209 and absorption effects (by Gaussian integration based upon the physical description of the crystal)
210 using the CrysAlis software package (Agilent, 2012). Further details pertaining to the data collection
211 protocols are given in Table 1.

212

213 The anisotropic structural refinements were performed using the SHELX-97 software (Sheldrick 1997)
214 starting from the atomic coordinates of Lucchesi et al. (1997). Neutral atomic scattering factors for O,
215 Al, Mn, and Fe were taken from the *International Tables for Crystallography* (Wilson and Prince

1999). The site population was modelled with two different protocols for galaxite and jacobsite, respectively, as described below. Secondary isotropic extinction effects were corrected according to the formalism of Larson (1967), as implemented in the SHELXL-97 package (Sheldrick 1997). Further details pertaining to the structure refinements are given in Table 1.

220

221

222 **4. Results**

223 *4.1 Galaxite*

224 The averaged chemical compositions of the synthetic galaxite samples are summarized in Table 2, with Mn valence estimated based on ensuring net neutrality with O²⁻ and Al³⁺. Samples GaAC, Ga93 and Ga90 all have similar chemical compositions, but are depleted in Al and O compared to stoichiometric galaxite. These three samples are closer in composition to spinels with 2:1 cations of Mn:Al. In contrast, Ga60 has near equal wt. % abundance of Mn and Al and a higher wt. % O than the other samples, with a composition more similar to end member galaxite with 2:1 cations of Al:Mn.

231

232 SC-XRD refinements for the galaxite samples (i.e., “GaAC”, “Ga93”, “Ga90”, “Ga60”, Table 1 and 3) were performed using a mixed Al/Mn- scattering curve at the *M* and *T* sites. The fraction of Al and Mn at both *M* and *T* sites was simultaneously refined. For all the data sets, convergence was rapidly achieved and the variance–covariance matrix did not show any significant correlation between the refined parameters. At the end of all the refinements, the residuals in the difference-Fourier maps of the electron density were less than $\pm 0.3 e^{-\text{\AA}^3}$, with agreement factors $R_1(F) < 0.02$ (with $F_o > 4\sigma(F_o)$ and 10 refined parameters, Table 1). For the sample “Ga93”, which showed a lower crystallinity as deduced based on the profile shape of the Bragg peaks, the residuals were $\pm 0.9 e^{-\text{\AA}^3}$, with

240 agreement factors $R_1(F) \sim 0.04$. Atomic positions, site occupancy factors (*s.o.f.*), displacement
241 parameters and bond distances are also reported in Table 1 and 3

242

243 XANES Mn K-edge data for the galaxite samples are shown in Fig. 1. The spectra for GaAC, 93 and 90
244 are all remarkably similar with a small, less defined shoulder on the rising edge (6551.5eV), followed
245 by the white line position at approximately 6557 eV and a slight shoulder around 6569 eV. In
246 comparison, the Ga60 spectrum has a more intense pre-edge peak, a much more defined peak on
247 the rising shoulder and a more defined peak following the main absorption crest (6569 eV). The
248 lower shoulder position may be associated with the white line peak position of Mn^{2+} , whilst the main
249 absorption peak is associated with Mn^{3+} . This suggests both the presence of Mn^{2+} and Mn^{3+} in the
250 galaxite samples. The more intense $1s-3d$ transition (pre-edge peaks) found in the spectrum for Ga60
251 suggests a larger proportion of Mn cations on *T* sites (Chalmin et al. 2009). XANES spectra for these
252 samples lack any characteristic features in the main edge and pre-edge peak region associated with
253 Mn^{4+} . The edge energy, white line position, and pre-edge centroid energy are all at a lower energy in
254 the galaxite samples than their positions in standards with Mn^{4+} (Farges 2005; Chalmin et al. 2009;
255 Manceau et al. 2012) so it was assumed that no Mn^{4+} was present, although the presence of minor
256 proportions of Mn^{4+} cannot be dismissed.

257

258 Peak fitting of the pre-edge peak for the galaxite samples, following background removal, show that
259 the $1s-3d$ transition peak can be modelled using one or two Gaussian peaks. The results of fitting are
260 shown in Table 4. The centroid energy for all Galaxite groups are within error of each other,
261 suggesting that the mean valence of Mn in all groups is the same. However, as identified from Fig. 1,
262 the pre-edge peak intensity varies between samples, suggesting that samples GaAC and Ga93 have
263 the least amount of Mn in tetrahedral coordination and Ga60 has the most.

264

265 4.2 *Jacobsite*

266 The averaged EMPA data for the three jacobsite runs (JcAC, Jc93, and Jc90, Table 2) show a decrease
267 in Fe and an increase in Mn under more reducing conditions. Sample JcAC is almost Mn free, and,
268 therefore, is expected to be similar in structure to magnetite (Fe_3O_4). Samples Jc93 and Jc90 are
269 closer in composition to ideal jacobsite, but Jc93 has excess Fe while Jc90 is deficient in Fe compared
270 to the ideal end member.

271 SC-XRD refinements for the jacobsite samples (JcAC, Jc93, and Jc90) were first performed using a
272 mixed Fe/Mn-scattering curve at the octahedral and tetrahedral sites, while the fraction of Fe and
273 Mn at the *M* and *T* sites were simultaneously refined. However, the similar X-ray scattering factors of
274 Fe and Mn led to a severe correlation between the refined Fe/Mn site populations. A different
275 strategy was then adopted, where site occupancies were modelled using the scattering curve of Fe
276 alone (i.e., the element with the highest scattering factor). The refined partial site occupancy
277 confirms the presence of a lighter element (i.e., Mn), and the refined *e*- content per site represents
278 the actual (Fe + Mn) contribute (Table 3). With this protocol, convergence was rapidly achieved on
279 all the data sets, and the variance–covariance matrix did not show any significant correlation
280 between the refined parameters. The quality of the refinements of the sample “JcAC” ($\pm 0.3 e^-/\text{\AA}^3$,
281 $R_1(F) \sim 0.01$) and “Jc93” ($\pm 0.5 e^-/\text{\AA}^3$, $R_1(F) \sim 0.02$) was slightly better than that of the sample “Jc90”
282 ($\pm 0.9 e^-/\text{\AA}^3$, $R_1(F) \sim 0.03$; Table 1). Atomic positions, site occupancy factors, displacement parameters,
283 and bond distances are also reported in Tables 1 and 3.

284

285 Stacked Fe K-edge XANES spectra for jacobsite samples are shown in Fig. 2. The absorption edge in
286 Jc90 and Jc93 plots between the edge position of Fe_3O_4 and Fe_2O_3 , suggesting the mean oxidation

287 state of iron may be greater than +2.6 in these samples. The K-edge of JcAC is similar to that of Fe₂O₃,
288 suggesting the mean valence state is close to +3, as would be expected.

289

290 The number, intensity, and centroid position of Gaussian/pseudo-Voigt components which can be
291 fitted to the *1s-3d* and *1s-4p* (quadrupolar and dipolar) electronic transitions that produce the Fe
292 pre-edge feature can be used to extract information on the coordination and average oxidation
293 state of Fe (Waychunas et al. 1986; Westre et al. 1997; Wilke et al. 2001). By comparing the Fe pre-
294 edge data to mineral standards where Fe is in a single valence, the average valence of iron can be
295 estimated if it is assumed that there is a linear trend between centroid energy and valence state.
296 Using tabulated values for mineral standards from Wilke et al. (2001), Fe oxidation state has been
297 estimated for the jacobsite samples. However, these are only approximations for the Fe redox state,
298 as when redox state and coordination change at the same time there is a considerable non-linearity
299 with redox and centroid position (Wilke et al. 2001).

300

301 Jc90 and Jc93 Fe K-edge pre-edge features can be fitted using two Gaussian functions. The centroid
302 position for these two functions were close to 7112.2 eV and 7113.2 eV. The JcAC spectrum required
303 fitting using four Gaussian functions, with two around 7113.45 eV and two further peaks with
304 centroid positions greater than 7115 eV, indicating either an environment around Fe which is either
305 tetrahedral or distorted octahedral (Pinakidou et al. 2006) or long-range order around Fe involving
306 *3d* orbitals of neighbouring iron atoms (Wilke et al. 2001). Therefore, the third and fourth peak were
307 excluded from calculating the mean centroid position and total integrated area. The pre-edge
308 averaged centroid position (Table 4) was compared to the variation of centroid position with redox
309 ratio of mixtures found in Wilke et al, (2001). The estimated Fe³⁺/ΣFe values were taken for the
310 mixtures of ^{IV}Fe²⁺/^{VI}Fe³⁺ which should give the maximum %Fe³⁺ for a given centroid position. JcAC
311 plots with 98% Fe³⁺, whilst there is approximately 74% Fe³⁺ in samples Jc93, and 70% Fe³⁺ in Jc90. The

312 integrated pre-edge intensity suggests that sample Jc90 contains greater proportions of Fe on the *M*
313 site compared to samples Jc93 and JcAC.

314

315 The Mn K-edge spectra for the jacobsite samples are shown at the bottom of Fig. 2. As with Fe K-
316 edge spectra shown in Fig. 2, samples Jc90 and Jc93 have a similar shape, but different intensities,
317 whereas the JcAC spectrum is shifted towards a higher absorption energy, which suggests Mn in this
318 sample, on average, is in a higher redox state. For samples Jc93 and Jc90 there is a slight peak on the
319 rising edge at approximately 6551 eV, which corresponds with the white line position of Mn²⁺
320 standards, and a further peak with the greatest intensity at 6556 eV, which is slightly lower than the
321 white line position of Mn³⁺ standards found over the energy range 6557-6559 eV. The pre-edge peak
322 for samples Jc93 and Jc90 can be modelled using three peaks whereas JcAC has to be modelled using
323 more functions. A triplet is suggestive of Mn³⁺ or Mn⁴⁺ being present in the 93 and 90 samples
324 (Farges 2005). The averaged Mn pre-edge peak centroid position is given in Table 4. The intensity of
325 the *1s-3d* transition suggests that Jc93 has greater amounts of *T* coordinated manganese than
326 samples JcAC or Jc90. The energy position of the Mn K-edge for the jacobsite samples suggests that
327 Jc90 and Jc93 consists of a mixture of Mn²⁺ and Mn³⁺, and its position close to a MnO standard
328 suggests that 2+ dominates in these samples . Whereas, the edge position of JcAC is greater than
329 Jc93 and Jc90, and is close to the edge position of a Mn₂O₃ standard, suggestive of Mn in an
330 oxidation state of 3+, or greater.

331

332 **5. Discussion**

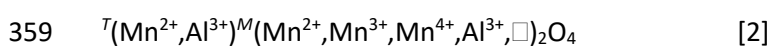
333 The single-crystal X-ray diffraction data of the galaxite and jacobsite samples provide unit-cell
334 constants and *u* parameters in agreement with those reported in the literature (*e.g.*, Bosi *et al.*, 2007;
335 Essene and Peacor, 1983; Lucchesi *et al.*, 1997; Hålenius *et al.*, 2007). In this class of minerals, the

336 length of the cell edge and the polyhedral bond distances are geometrically related, which in turn
 337 reflects the degree of cation ordering among the *T* and *M* sites. The structure refinements converged
 338 with a ratio of the displacement parameters of the *T*, *M*, and oxygen sites (*i.e.*, $U_{\text{eq}}(T):U_{\text{eq}}(M):U_{\text{eq}}(O)$),
 339 where U_{eq} is the equivalent isotropic atomic displacement parameter and is defined as a third of the
 340 trace of the orthogonalized matrix U_{ij} , which describes the anisotropic displacement ellipsoid)
 341 comparable to the literature data for these two spinels. Refined Al/Mn-fractions at the *M* and *T* sites
 342 in galaxite reflect the actual distribution of the two cations. In contrast, the Fe-fraction at the *M* and
 343 *T* sites in jacobsite is only “virtual” and reflects the electron content per site due to the co-presence
 344 of Fe and Mn. The calculated sum of the electron content at the *T* and *M* sites on the basis of the
 345 multi-element distribution obtained by the X-ray structure refinements and by bond length
 346 modelling/EMPA are given in Table 3. We defined the parameter $\Delta(\Sigma e_{\text{p.f.u.}})\%$ as the difference of
 347 the total *e*- number (per formula unit) between the values obtained by the X-ray structure
 348 refinements and by bond length modelling/EMPA. This parameter provides an assessment of the
 349 consistency between the results obtained by the different experimental methods used here.

350

351 *5.1 Cation distribution in Galaxite*

352 Hålenius et al. (2007) reported a stoichiometric synthetic manganese aluminate (MnAl_2O_4) which has
 353 a partial inverse spinel structure with an inversion parameter, $i = 0.1$, with Mn^{2+} strongly ordered on
 354 the *T* site. However, the degree of inversion for other natural and synthetic spinels is likely to be
 355 dependent on the method of preparation (Schreyeck et al. 2001; Carta et al. 2008), thermal history
 356 (Ball et al. 2005, Andreozzi et al. 2000), as well as the chemical composition of the spinel (Carta et al.
 357 2009, Andreozzi et al. 2001). Thermodynamic models of cubic spinel in the Al-Mn-O system suggests
 358 that a generalized form for this system is (Chatterjee and Jung 2014):



360 whereas, in the case of tetragonal Al-Mn-O spinels, Mn²⁺ and Mn³⁺ can occupy both the *T* and *M*
361 sites. Because the galaxite samples only have one multivalent element, and by assuming that Mn⁴⁺ is
362 not present in these samples, the Mn³⁺/Mn²⁺ ratio can be calculated from the compositional average
363 point analyses and the SC-XRD data, ensuring net electrical neutrality. Charge balance of the spinel
364 structure can be used in the galaxite samples to determine the proportion of Mn²⁺ and Mn³⁺ cations
365 present in each sample (i.e. the average Mn valence). The distribution of these Mn cations can then
366 be established by ensuring the distribution between the *M* and *T* sites simultaneously satisfies the
367 following two parameters: 1. The mean atomic number (m.a.n.) for each site, as defined by:

368

$$369 \quad m. a. n. _T = \sum_i {}^{IV}X_i N_i \quad [3]$$

370

$$371 \quad m. a. n. _M = \sum_i {}^{VI}X_i N_i \quad [4]$$

372

373 where X_i is the fraction of the cation species in the *T* and *M* sites, and N_i is their atomic number.

374

375 And, 2. The polyhedral bond length, calculated from a linear combination of each cation species
376 cation-oxygen bond distances from end member spinels:

377

$$378 \quad T - O = \sum_i {}^{IV}X_i {}^{IV}D_i \quad [5]$$

379

$$380 \quad M - O = \sum_i {}^{VI}X_i {}^{VI}D_i \quad [6]$$

381

382 where ${}^{IV}Di$ and ${}^{VI}Di$ is the cation to oxygen bond distance of each cation in the T and M sites,
383 respectively.

384 The X-ray structure refinement data (Table 3) already satisfies equations 3 and 4, so by applying
385 equations 5 and 6, the distribution of Mn^{2+} and Mn^{3+} can be determined. The distribution of cations
386 across the T and M sites was calculated using the cation-oxygen bond lengths listed in Table 5.
387 Determining cation distribution is made simpler by first assuming that Mn^{3+} cations are found on the
388 M sites, because of the strong preference for Mn^{2+} for the T site (Chatterjee and Jung 2014).
389 However, it was found that to model Ga60, considerable amounts of Mn^{3+} were needed on the
390 tetrahedral site (≈ 0.2 cations p.f.u.) to satisfy the particularly short $T-O$ bond length.

391

392 The final structural refinement with cation distribution is given in Table 3. When modelling mean $T-O$
393 and $M-O$ bond lengths, anything less than 0.02\AA was considered an acceptable fit (Lavina et al. 2002).
394 Calculated $M-O$ bond lengths for the distribution of cations, including oxidation state, are in good
395 agreement with the observed values from the SC-XRD data, giving $\Delta(M-O) \leq 0.001\text{\AA}$ for all but the
396 Ga60 sample, where $\Delta(M-O) = 0.007\text{\AA}$. However, the presence of a large residual for $\Delta(T-O)$ for **GaAC,**
397 **Ga93, and Ga90** $T-O$ bond lengths ($\leq 0.025\text{\AA}$), **when using the 2.04\AA ${}^{IV}Mn^{2+}$ T-O bond length from**
398 **Lavina et al. (2002) is unsatisfactory.** This difference from the observed and predicted size of the T-O
399 bond, in the galaxite samples, may suggest that a correction function is required. **Hålenius et al.**
400 **(2011), suggests the ${}^{IV}Mn-O$ bond length for a fully ordered end-member galaxite is 2.05\AA . Using**
401 **2.05\AA for ${}^{IV}Mn^{2+}$ T-O bond length lowers the $\Delta(T-O)$ residual for all $T-O$ bond lengths to less than 0.02**
402 **\AA .** It is likely that the **large structural relaxation** is linked to cation occupancy on the M site, which
403 not only alters the $M-O$ bond length, but also changes the octahedral angle $O-M-O$, lengthening the
404 tetrahedral distance (Bosi et al., 2011). Distortion of the octahedral site from cubic to tetragonal
405 symmetry, due to the Jahn-Teller effect, is expected with increasing concentration of Mn^{3+} in 6-fold
406 coordination. However, an overall lowering of the space group from $Fd\bar{3}m$ to $I4_1/amd$ is unlikely

407 unless concentrations of $^{VI}Mn^{3+}$ exceed 1.4_{apfu} (Lucchesi et al. 1997). Additional terms have to be
408 added to equation 5 to describe the effect that cation speciation, on the octahedral site, has on the
409 T-O bond lengths (Lavina et al. 2002).

410

$$411 \quad T - O = \sum_i {}^{IV}X_i {}^{IV}D_i + k_1 {}^{VI}X_z \quad [7]$$

412

413 Where the coefficient k_1 is added to account for the effect of cation X_z in the M site (where z is an
414 element which alters the O-M-O bond angle).

415

416 The inversion parameters for samples GaAC, Ga93, and Ga90 are between 0.154 and 0.18 which is
417 slightly larger than the 0.1 suggested by Hålenius et al. (2007). Whereas the inversion parameter for
418 sample Ga60 is closer to 0.2. Whilst both the synthetic spinels in our study and those in Hålenius et
419 al. (2007) were flux grown in a borax flux at a final temperature of 900 °C, our study cooled at a
420 faster rate (12.5 °C/hr compared to 4 °C/hr) from peak T, did not contain a surplus of Al_2O_3 to
421 prevent the formation of trivalent manganese, and were synthesized in more oxidized conditions
422 (with the exception of Ga60). Additionally, whilst our samples were fast quenched in water and air,
423 the quenching technique in Hålenius et al. (2007) only mentions runs were completed with fast
424 cooling to ambient temperature, hence this quenching technique may not preserve initial cation
425 order (or disorder). These differences in experimental procedures may account for the differing
426 inversion factor and galaxite compositions between our study and Hålenius et al. (2007).

427

428 *5.3 Determining the oxidation state of Fe and Mn using XANES, EMPA and SC-XRD*

429 Cation distribution and oxidation information, from the galaxite samples, can be used to compare
430 how satisfactory existing methods of predicting average valence and coordination from XANES
431 spectra compare. Combining EMPA, XANES, and SC-XRD data for samples where there is a sufficient
432 difference in the scattering factors of the cations (*e.g.* galaxite spinels) can satisfactorily determine
433 the structure of a spinel structure. Furthermore, bond length modelling in these types of samples
434 can be used to assign cations across the *T* and *M* sites. However, for spinels where there may be
435 significant oxygen deficiency, cation vacancies and/or the scattering of the cation ions are too similar
436 meaning there are too many variables to correctly assign cation valence distributions across the *T*
437 and *M* sites (*e.g.* manganese ferrites).

438

439 The SC-XRD data and stoichiometric calculations of the EMPA data result in slightly different crystal
440 compositions (hence different mean oxidation state) for each galaxite sample. EMPA data suggests
441 the mean valence of Mn in the galaxite samples is 2.51, 2.53, 2.50 and 2 respectively for samples
442 GaAC, Ga93, Ga90 and Ga60. Whereas, the oxidation state of Mn implied by the SC-XRD data (Table
443 3) suggests Mn in all samples has an average valence of ≈ 2.41 (obtained excluding Ga60).

444

445 XANES data can be used to determine the oxidation state of Mn and Fe. One common method of
446 determining the average valence and coordination of atoms is by examining the pre-edge peak
447 region of XANES spectra. The pre-edge peak is a manifestation of the $1s-3d$ transition in transitional
448 metals. Fitting this pre-edge provides what is becoming the preferred technique to obtain
449 quantitative data on cation valence and coordination information from XANES spectra. Other
450 features in XANES spectra which give an indication of the oxidation state of the absorbing atom are
451 white line position and/or the position of the absorption edge. However, these features are highly
452 sensitive to local environment and long-range ordering, and so, are not suitable to quantitatively
453 determine mean oxidation state or coordination. Charge balance and bond length modelling of the

454 SC-XRD data indicates the likely individual cation charges and coordination in the galaxite samples
455 (Table 3). The next step is to identify how well the valence/coordination information from XRD
456 matches those obtained from pre-edge fitting of synchrotron data.

457

458 A test of how well Mn K edge XANES data can be used to determine oxidation state is to compare
459 centroid position of the pre-edge peak for the galaxite samples (Table 4), where mean oxidation
460 state has been estimated by EMPA or SC-XRD, to the pre-edge peak of samples with known
461 oxidation state. To compare this dataset to other published studies, we first assessed how the
462 centroid position and intensity in single valence standards collected during this beamline session and
463 a previous session (Bromiley et al., 2015) compared to those in Chalmin et al. (2009). The centroid
464 position of standards in this study and Chalmin et al. (2009) agreed within $\pm 0.09\text{eV}$. However, when
465 comparing the position of the pre-edge peaks for the galaxite samples (where the estimated valence
466 is either 2.41 SC-XRD, or 2.51 EMPA) the centroid position of these samples should be $\approx 6539.47\text{eV}$
467 according to Chalmin et al. (2009), compared to the measured value of 6539.04eV (discrepancy of
468 0.43eV). This question whether we can use a small set of oxide standards to calculate average
469 valences in oxides of differing composition. This study highlights the current inability to accurately
470 determine the oxidation state/coordination of atoms using the $1s-3d$ pre-edge peak found on a Mn K
471 edge XANES spectrum. Part of this difficulty in determining the oxidation state of Mn using the pre-
472 edge peak may be due to the small energy difference in centroid position between $\text{Mn}^{2+}/\text{Mn}^{3+}$
473 (0.35eV) and $\text{Mn}^{3+}/\text{Mn}^{4+}$ (0.55eV). The way XANES data is processed and fitted may also produce
474 unambiguity in Mn valence.

475

476 Pre-edge peak fitting of the Fe K-edge has been successfully in evaluating the $\text{Fe}^{3+}/\sum\text{Fe}$ ratio in
477 silicate glass (Berry et al. 2003; Cottrell et al. 2009). Calculating the average valence of Fe in minerals
478 remains challenging due to the need to accurately calibrate XANES spectra for each system

479 investigated (Berry et al. 2010). Factors limiting the use of XANES in determining the oxidation state
480 of multivalent elements in minerals include: the restricted range of Fe^{2+} and Fe^{3+} found in most
481 minerals, the effect of compositional variability and particularly the effect that crystal orientation
482 has on the collected spectra, and the difficulties in background fitting. In many cases, the oxidation
483 state of redox variable elements tends to be quantified by the weak $1s \rightarrow 3d$ pre-edge, although this
484 edge, and particular spectral backgrounds to pre-edge features, are also sensitive to changes in
485 coordination, site symmetry and composition (Doyle et al. 2016). Knowing the cation coordination in
486 a sample is vital in determining the oxidation state of an unknown as shown by the variation of
487 centroid position with redox ratio of mixtures found in Wilke et al. (2001). A suite of well
488 documented Fe spinels may provide the means to explore and quantify further the effects that Fe
489 oxidation state and coordination have on the shape of a XANES spectrum due to the varying ratio of
490 $\text{Fe}^{3+}/\Sigma\text{Fe}$ found in many spinels and the different degrees of inversion found in many spinels.

491

492 An alternative way to determine Mn redox states from XANES data is linear combination fitting (LCF)
493 of single valence standards with similar structures to the mixed valent sample (Manceau et al. 2012;
494 Bromiley et al. 2015), where the resulting fit indicates the relative proportions of each oxidation
495 state present in the unknown sample. Linear combination fitting is reliant on the unknown having
496 the absorbing element in similar coordination to the standard. This is problematic in spinels as Fe
497 and Mn in these samples may exist in two different coordination environments with variable
498 distributions between both sites and these elements may also be present in multiple oxidations
499 states in the same or different sites; therefore, it is unlikely that LCF will give accurate results.
500 Furthermore, it is often difficult to acquire well documented standards where each oxidation state
501 of Mn/Fe is present in all necessary coordination environments. As a first approximation, Mn
502 average valence for the galaxite samples was determined by fitting the spectra with a linear
503 combination fit (LCF) of MnO and Mn_2O_3 spectra in the region between 6520 and 6570 eV. This

504 resulted in a mean Mn valence of 2.52, 2.51 and 2.55 for samples GaAC, Ga93, and Ga90,
505 respectively, and an average oxidation state of 2.26 for Ga60. These estimated averaged oxidation
506 states are close to those estimated from EMPA (Table 2), with the exception of Ga60, and generally
507 higher than those estimated based on SD-XRD data (Table 3). Therefore, LCF, both estimates higher
508 average Mn valence, and indicates a change in valence in the most reduce sample (Ga60) which is
509 not apparent from other data. LCF of jacobsite samples suggests that the oxidation state of Mn in
510 JcAC is approximately 3+, whilst in Jc93 and Jc90 the oxidation state is 2.3 and 2.4 respectively.

511 Analysis of the full EXAFS spectrum may be an alternate way to determine site occupancies,
512 although this requires *ab. initio* calculations to produce standards by which sample spectra can be
513 compared. Although EXAFS analysis of jacobsite has been carried out by various groups (Yang et al.
514 2004; Kodre et al. 2008; Carta et al. 2009) it remains uncertain as to whether this procedure could be
515 used for more complex solid solutions.

516

517 *5.4 Cation distribution in Mn spinel as a function of fO_2*

518 SC-XRD refinements from individual galaxite crystals suggest a decrease in $T\text{Mn}^{2+}$ and $M\text{Mn}^{3+}$ with a
519 reduction in oxygen fugacity, whilst Al^{3+} (*M* site and *T* site) and Mn^{2+} (*T* site) increase. These SC-XRD
520 findings are in contrast to the EMPA data which suggest there should be a slight decrease in Al
521 cations p.f.u. with more reduced conditions. The trend difference between these two sets of data
522 may be due in part to EMPA data being measured on multiple crystals whereas SC-XRD data was
523 measured on an individual crystal from a batch, selected based on size and lack of twinning.

524

525 EMPA data from jacobsite samples suggests that oxygen fugacity affects partitioning of Mn and Fe
526 between the sodium tetraborate flux and spinel crystals, such that total Mn content in spinel
527 increases, and Fe content decreases, with more reducing conditions. This contrasts with the $\text{Log } fO_2$ -

528 T diagram from Bonsdorf et al. (1998) that would suggest that Fe-rich spinel should dominate under
529 more reduced conditions. The progressive enrichment of Mn-rich spinels with lowering fO_2 in this
530 study, compared to Bonsdorf et al. (1998), may highlight an effect of different routes of synthesis.
531 An additional effect of reduction for the jacobsite spinels is a decrease in the estimated valence of Fe
532 from approximately 3+ to ~2.7+ between samples AC and 93/90. Also, there is a significant
533 lengthening of the M-O bonds between samples AC/93 and 90 which would indicate the
534 replacement of Fe^{3+}/Mn^{3+} with Mn^{2+}/Fe^{2+} . Yamanaka and Nakahira (1973) noted that a decrease in
535 fO_2 resulted in a decrease in the lattice parameter with fO_2 , whereas, in this study, the most reduced
536 sample has the largest lattice parameter. Differences between this study and Yamanaka and
537 Nakahira (1973) may be because their experiments were carried out using solid state reactions
538 whereas here mineral composition is not nominally fixed but varies as a function of the behaviour of
539 the borax flux.

540

541 The oxygen fugacity for runs Ga93/Jc93 and Ga90/Jc90 equates to IW +2.5 and +2.9 respectively.
542 These values span fO_2 ranges which are expected for Martian rocks (e.g. nahklites and chassingnites
543 - Wadhwa 2008, Righter et al. 2016) as well as primitive basaltic rocks found on Earth (Righter et al.
544 2016). The coupled variation of Fe and Mn found in the jacobsite samples run at IW +2.5 and +2.9
545 could have potential for helping to constrain the redox conditions of Martian and terrestrial basalts
546 with further study.

547

548 This study suggests that there may be an observable change in the partitioning of Mn between Mn-
549 Fe-O spinel and silicate melt. A recent study by Wijbrans et al. (2015), on the influence of
550 composition and oxygen fugacity on spinel-melt partitioning, found that Mn is slightly incompatible
551 in spinel. They noted no observable effect on the partitioning of Mn with redox and change in
552 temperature, but did observe a slight compositional effect, with higher partition coefficients for Mn

553 in Fe²⁺-rich spinels compared to Mg-rich spinels. This further indicates the complex interplay
554 between partitioning behaviour, site occupancy, site distortion, and crystal chemistry in spinel group
555 minerals. As such, although investigation of end-member compositions may provide insight into the
556 distribution and ordering of multi-valent elements in spinels, data cannot readily be applied to
557 modelling the effects of external influences such as fO_2 on valence state of Fe, and in particular, Mn.

558

559 **6. Concluding remarks**

560 Mn-Fe bearing spinels may have the potential to determine fO_2 conditions for the parental melt they
561 formed, by recording the effects of fO_2 on element distribution (partitioning and site ordering). This
562 may be due to lengthening of the $M-O$ bond length in sample Jc90 which may result from a change in
563 the cation oxidation state or species on the M site under more reducing fO_2 . However, decoupling
564 the effects of temperature and oxygen fugacity on $^{55}\text{Fe}^{3+}$ - $^{55}\text{Mn}^{2+}$ exchange in jacobsite spinels is non-
565 trivial. Furthermore, determining the mean oxidation state and coordination environment of Fe and
566 Mn in spinels using XANES remains challenging if both the oxidation state and coordination of the
567 absorbing atom changes between samples and standards. Additional insight into spinel crystal
568 chemistry can be provided by comparing results of compositional analyses, XANES and SC-XRD
569 refinements, although difficulties in modelling Mn XANES spectra mean that this approach is better
570 suited to constraining the crystal chemistry of end-member compositions, rather than complex,
571 naturally occurring spinels. In contrast to jacobsite, Mn content in galaxite spinels shows little if not
572 no change with varying oxidation conditions of synthesis, implying that element partitioning in spinel
573 is compositionally and structurally dependent. This indicates that variation in Mn valence in spinel is
574 largely driven by changes in Fe valence, presumably via the exchange $\text{Mn}^{2+} + \text{Fe}^{3+} \rightleftharpoons \text{Mn}^{3+} + \text{Fe}^{2+}$.

575

576 The reason for non-stoichiometry in the samples remains unclear. Only the most reduced galaxite
577 sample is close to stoichiometric, with more oxidized samples Al-deficient and Mn-rich. Unlike the
578 findings of Bosi et al. (2007) on Mg-Mn-Al spinels, we see no increase in trivalent Mn on the *T* site
579 with more oxidized conditions based on bond length modelling (Table 3). XANES data indicate that
580 valence of Mn is substantially higher than 2 in the oxidized samples. This might be explained by the
581 observed relative partitioning of Mn²⁺ onto the *T* site; Mn³⁺ is more readily incorporated onto the *M*
582 site, where it competes with Al³⁺. As a consequence, more oxidized samples are more Mn-rich. In
583 Ga60, more reducing conditions favour Mn²⁺, and therefore, galaxite compositions are close to
584 stoichiometric. SC-XRD data are consistent with an increase in the proportion of ⁵⁵Mn in Ga60,
585 although a substantial change in average Mn valence is not observed in XANES data; in fact, it is
586 likely that XANES data do not reveal any change in Mn valence across the galaxite samples.

587

588 Redox conditions used during synthesis imply JcAC should contain only Fe³⁺, consistent with XANES
589 data, and that Fe should be mixed valence in Jc93 and Jc90. Trends in determined Fe average
590 valence are consistent with imposed *fO*₂ conditions. According to the exchange Mn²⁺ + Fe³⁺ ⇌ Mn³⁺ +
591 Fe²⁺, increase in proportion of Fe²⁺ should result in an increase in the proportion of Mn³⁺. However,
592 between samples Jc93 and Jc90 there is no obvious change in the Mn K-edge spectra suggestive of
593 an increase in Mn valence. Decrease in *fO*₂ for jacobsite samples results in an increase in Mn
594 contents and decrease in Fe contents. In contrast to galaxite, stoichiometric jacobsite appears to
595 form at intermediate *fO*₂ conditions. Again, it is unclear what the driving force for this compositional
596 change might be. However, it is logical that stoichiometric jacobsite is stable under intermediate
597 redox conditions, as it nominally contains Mn²⁺ and Fe³⁺. Under more reducing conditions, the
598 average valence of Fe decreases. Partially disordered jacobsite can form a partial solid solution series
599 with magnetite, Fe²⁺Fe³⁺₂O₄, which has an inverse spinel structure. As such, the 3+ Fe is expected to
600 readily substitute onto the *T* site in jacobsite. The observed preference for Mn²⁺ to be incorporated

601 onto the *T* site in spinels would, in combination with the ability for Fe to be incorporated onto either
602 site, explain why jacobsite samples here are non-stoichiometric and Fe-rich. Under the most reduced
603 conditions under which jacobsite is stable (i.e. Jc90), crystals become in turn non-stoichiometric and
604 Mn-rich. This might again relate to an increase in proportion of Mn²⁺, although this remains
605 unsupported by XANES data.

606 Combined XANES and SC-XRD data may provide mixed valent and mixed coordination standards for
607 future studies. This includes spinels such as galaxite where there is less ambiguity in the final refined
608 structure than jacobsite, where the similar scattering of Fe and Mn makes correct valence and
609 coordination assignment much more difficult without additional data such as Mössbauer or neutron
610 diffraction data. However, the relationship between composition, site occupancy and Fe and Mn
611 valence in spinels is complex and interdependent. **Additional effects of variables such as mineral-**
612 **melt partitioning, temperature, and pressure, also, still need to be assessed before the development**
613 **of a Mn-Fe oxy-geobarometer.** As such, development of an oxy-barometer based on spinel crystal
614 chemistry is non-trivial.

615

616 **Acknowledgements**

617 The authors acknowledge the experimental and analytical facilities at The University of Edinburgh,
618 The University of Milan and The University of Bristol. We thank Chris Hayward and Benjamin Buse
619 for assistance with EMP analyses, Diamond Light Source for access to beamline I18 (Sp10070), and
620 Fred Mosselmans for assistance with XANES measurements. This work was funded by a NERC DTP
621 grant (Grant award code NE/L002558/1).

622 **References**

623 Agilent (2012) Xcalibur CCD system. CrysAlis software system.

- 624 Allen, G.C., Jutson, J.A., and Tempest, P. A. (1988) Characterisation of Manganese-Chromium-Iron
625 Spinel-Type Oxides. *Journal of Nuclear Materials*, 160, 34–47.
- 626 Andreozzi, G.B. (1999) Synthetic spinels in the (Mg, Fe²⁺, Zn)(Al, Fe³⁺)₂O₄ system : I . Flux growth of
627 single crystals. *Periodico di Mineralogia*, 68, 43–51.
- 628 Andreozzi, G.B., Princivale, F., Skogby, H., and Della Giusta, A. (2000) Cation ordering and structural
629 variations with temperature in MgAl₂O₄ spinel: An X-ray single-crystal study. *American Mineralogist*,
630 85, 1164–1171.
- 631 Andreozzi, G.B., Lucchesi, S., Skogby, H., and Della Giusta, A. (2001) Compositional dependence of
632 cation distribution in some synthetic (Mg,Zn)(Al,Fe³⁺)₂O₄ spinels. *European Journal of Mineralogy*, 13,
633 391 LP-402.
- 634 Anthony, J.W., Bideaux, R.A., Bladh, K.W., and Nichols, M.C. (1997) Handbook of Mineralogy: Halides,
635 Hydroxides, Oxides. Mineral Data Publishing.
- 636 Arai, S. (1992) Chemistry of chromian spinel in volcanic rocks a potential guide to magma chemistry.
637 *Mineralogical Magazine*, 56, 173–184.
- 638 Arató, R., and Audétat, A. (2017) Vanadium magnetite--melt oxybarometry of natural, silicic magmas:
639 a comparison of various oxybarometers and thermometers. *Contributions to Mineralogy and*
640 *Petrology*, 172, 52.
- 641 Ball, J.A., Pirzada, M., Grimes, R.W., Zacate, M.O., Price, D.W., and Uberuaga, B.P. (2005) Predicting
642 lattice parameter as a function of cation disorder in MgAl₂O₄ spinel. *Journal of Physics: Condensed*
643 *Matter*, 17, 7621–7631.
- 644 Barnes, S.J., and Roeder, P.L. (2001) The range of spinel compositions in terrestrial mafic and
645 ultramafic rocks. *Journal of Petrology*, 42, 2279–2302.

646 Battault, T., Legros, R., and Rousset, A. (1995) Structural and electrical properties of iron manganite
647 spinels in relation with cationic distribution. *Journal of the European Ceramic Society*, 15, 1141–1147.

648 Battault, T., Legros, R., and Rousset, A. (1995) Structural and electrical properties of iron manganite
649 spinels in relation with cationic distribution. *Journal of the European Ceramic Society*, 15, 1141–1147.

650 Berry, A.J., O'Neill, H.S.C., Jayasuriya, K.D., Campbell, S.J., and Foran, G.J. (2003) XANES calibrations
651 for the oxidation state of iron in a silicate glass. *American Mineralogist*, 88, 967–977.

652 Berry, A.J., Yaxley, G.M., Woodland, A.B., and Foran, G.J. (2010) A XANES calibration for determining
653 the oxidation state of iron in mantle garnet. *Chemical Geology*, 278, 31–37.

654 Biagioni, C., and Pasero, M. (2014) The systematics of the spinel-type minerals : An overview.
655 *American Mineralogist*, 99, 1254–1264.

656 Bonsdorf, G., Schäfer, K., Teske, K., Langbein, H., and Ullmann, H. (1998) Stability region and oxygen
657 stoichiometry of manganese ferrite. *Solid State Ionics*, 110, 73–82.

658 Bosi F, Andreozzi GB, Hålenius U, Skogby H (2011) Zn-O tetrahedral bond length variations in normal
659 spinel oxides. *American Mineralogist*, 96, 594–598

660 Bosi, F., Hålenius, U., Andreozzi, G. B., Skogby, H., & Lucchesi, S. (2007). Structural refinement and
661 crystal chemistry of Mn-doped spinel: A case for tetrahedrally coordinated Mn³⁺ in an oxygen-based
662 structure. *American Mineralogist*, 92(1), 27–33.

663 Bromiley, G.D., Gatta, G.D., and Stokes, T. (2015) Manganese incorporation in synthetic hercynite.
664 *Mineralogical Magazine*, 79, 635–647.

665 Burger, P. V., Shearer, C.K., Papike, J., Bell, A.S., and Muttik, N. (2016) Igneous spinel chemistry as a
666 function of temperature and oxygen fugacity in martian melts. *47th Lunar and Planetary Science
667 Conference*, 6–7.

668 Canil, D. (1999) Vanadium partitioning between orthopyroxene, spinel and silicate melt and the
669 redox states of mantle source regions for primary magmas. *Geochimica et Cosmochimica Acta*, 63,
670 557–572.

671 Carta, D., Casula, M.F., Falqui, A., Loche, D., Mountjoy, G., Sangregorio, C., and Corrias, A. (2009) A
672 Structural and magnetic investigation of the inversion degree in ferrite nanocrystals MFe_2O_4 (M = Mn,
673 Co, Ni). *Journal of Physical Chemistry C*, 113, 8606–8615.

674 Carta, D., Casula, M.F., Floris, P., Falqui, A., Mountjoy, G., Boni, A., Sangregorio, C., and Corrias, A.
675 (2010) Synthesis and microstructure of manganese ferrite colloidal nanocrystals. *Physical Chemistry
676 Chemical Physics*, 12, 5074–5083.

677 Carta, D., Casula, M.F., Mountjoy, G., and Corrias, A. (2008) Formation and cation distribution in
678 supported manganese ferrite nanoparticles: an X-ray absorption study. *Physical Chemistry Chemical
679 Physics*, 10, 3108–3117.

680 Carta, D., Marras, C., Loche, D., Mountjoy, G., Ahmed, S.I., and Corrias, A. (2013) An X-ray absorption
681 spectroscopy study of the inversion degree in zinc ferrite nanocrystals dispersed on a highly porous
682 silica aerogel matrix. *Journal of Chemical Physics*, 138.

683 Chalmin, E., Farges, F., and Jr, G.E.B. (2009) A pre-edge analysis of Mn K-edge XANES spectra to help
684 determine the speciation of manganese in minerals and glasses. *Contributions to Mineralogy and
685 Petrology*, 157, 111–126.

686 Chatterjee, S., and Jung, I.H. (2014) Critical evaluation and thermodynamic modeling of the Al-Mn-O
687 (Al_2O_3 -MnO-Mn₂O₃) system. *Journal of the European Ceramic Society*, 34, 1611–1621.

688 Cookenboo, H.O., Bustin, R.M., and Wilks, K.R. (1997) Detrital chromian spinel compositions used to
689 reconstruct the tectonic setting of provenance: implications for orogeny in the Canadian Cordillera.
690 *Journal of Sedimentary Research*, 67, 116–123.

691 Cottrell, E., Kelley, K. A., Lanzirotti, A., and Fischer, R. A. (2009) High-precision determination of iron
692 oxidation state in silicate glasses using XANES. *Chemical Geology*, 268, 167–179.

693 Deines, P., Nafziger, R.H., Ulmer, G.C., and Woermann, E. (1974) Temperature-oxygen fugacity tables
694 for selected gas mixtures in the system CHO at one atmosphere total pressure. *Bulletin of the Earth
695 and Mineral Sciences*, 88.

696 Doyle, P.M., Berry, A.J., Schofield, P.F., and Mosselmans, J.F.W. (2016) The effect of site geometry ,
697 Ti content and Ti oxidation state on the Ti K-edge XANES spectrum of synthetic hibonite. *Geochimica
698 et Cosmochimica Acta*, 187, 294–310.

699 Farges, F. (2005) Ab initio and experimental pre-edge investigations of the Mn K-edge XANES in
700 oxide-type materials. *Physical Review B*, 71, 155109.

701 Fleet, M.E. (1981) The structure of magnetite. *Acta Crystallographica Section B Structural
702 Crystallography and Crystal Chemistry*, 37, 917–920.

703 Hålenius, U., Bosi, F., and Skogby, H. (2007) Galaxite, $MnAl_2O_4$, a spectroscopic standard for
704 tetrahedrally coordinated Mn^{2+} in oxygen-based mineral structures. *American Mineralogist*, 92,
705 1225–1231.

706 Hålenius, U., Bosi, F. and Skogby, H. (2011) A first record of strong structural relaxation of TO_4
707 tetrahedra in a spinel solid solution. *American Mineralogist*, 96, 617–622. Mineralogical Society of
708 America.

709 Haskel D (1999) The FLUO package.

710 Henderson, C.M.B., Pearce, C.I., Charnock, J.M., Harrison, R.J., and Rosso, K.M. (2016) An X-ray
711 magnetic circular dichroism (XMCD) study of Fe ordering in a synthetic $MgAl_2O_4 - Fe_3O_4$ (spinel –
712 magnetite) solid solution series; implications for magnetic properties. *American Mineralogist*, 101,
713 1373–1388.

714 Herranz, T., Rojas, S., Ojeda, M., Pérez-Alonso, F.J., Terreros, P., Pirota, K., and Fierro, J.L.G. (2006)
715 Synthesis, Structural Features, and Reactivity of Fe–Mn Mixed Oxides Prepared by Microemulsion.
716 *Chemistry of Materials*, 18, 2364–2375.

717 Kim, D.-H., Zeng, H., Ng, T.C., and Brazel, C.S. (2009) T1 and T2 relaxivities of succimer-coated
718 $MFe_2^{3+}O_4$ (M=Mn²⁺, Fe²⁺ and Co²⁺) inverse spinel ferrites for potential use as phase-contrast agents in
719 medical MRI. *Journal of Magnetism and Magnetic Materials*, 321, 3899–3904.

720 Kodre, A., Arcon, I., Padeznik Gomilsek, J., and Makovec, D. (2008) An Expanded EXAFS Model of Mn,
721 Zn, and Fe Spinel Nanoparticles. *Acta chimica slovenica*, 55, 125–131.

722 Kraft S, Stümpel J, Becker P, Kuetgens U (1996) High resolution x-ray absorption spectroscopy with
723 absolute energy calibration for the determination of absorption edge energies. *Review of Scientific*
724 *Instruments*, 67, 681 – 687

725 Larson, A.C. (1967) Inclusion of secondary extinction in least-squares calculations. *Acta*
726 *Crystallographica*, 23, 664–665.

727 Lavina, B., Salviulo, G. and Giusta, A. Della. (2002) Cation distribution and structure modelling of
728 spinel solid solutions. *Physics and Chemistry of Minerals*, 29, 10–18.

729 Lu, J., Ma, S., Sun, J., Xia, C., Liu, C., Wang, Z., ... Gu, Z. (2009). Manganese ferrite nanoparticle
730 micellar nanocomposites as MRI contrast agent for liver imaging. *Biomaterials*, 30(15), 2919–2928.

731 Lucchesi, S., Russo, U., and Della Giusta, A. (1997) Crystal chemistry and cation distribution in some
732 Mn-rich natural and synthetic spinels. *European Journal of Mineralogy*, 9, 31–42.

733 Manceau, A., Marcus, M., and Grangeon, S. (2012) Determination of Mn valence states in mixed-
734 valent manganates by XANES spectroscopy. *American Mineralogist*, 97, 816–827.

735 Pinakidou, F., Katsikini, M., Paloura, E.C., Kavouras, P., Kalogirou, O., Komninou, P., Karakostas, T.,
736 and Erko, A. (2006) On the coordination environment of Fe- and Pb-rich solidified industrial waste:
737 An X-ray absorption and Mössbauer study. *Journal of Non-Crystalline Solids*, 352, 2933–2942.

738 Ravel, B., and Newville, M. (2005) ATHENA, ARTEMIS, HEPHAESTUS: data analysis for X-ray
739 absorption spectroscopy using IFEFFIT. *Journal of Synchrotron Radiation*, 12, 537–541.

740 Redfern, S.A.T., Harrison, R.J., O’Neill, H.S.C., and Wood, D.R.R. (1999) Thermodynamics and kinetics
741 of cation ordering in $MgAl_2O_4$ spinel up to 1600 degrees C from *in situ* neutron diffraction. *American*
742 *Mineralogist*, 84, 299–310.

743 Righter, K., Leeman, W.P., and Hervig, R.L. (2006) Partitioning of Ni, Co and V between spinel-
744 structured oxides and silicate melts: Importance of spinel composition. *Chemical Geology*, 227, 1–25.

745 Righter, K., Sutton, S. R., Danielson, L., Pando, K., & Newville, M. (2016). Redox variations in the inner
746 solar system with new constraints from vanadium XANES in spinels. *American Mineralogist*, 101(9),
747 1928-1942.

748 Roeder, P.L. (1994) Chromite: from the fiery rain of chondrules to the Kilauea Iki lava lake. *Canadian*
749 *Mineralogist*, 32, 729–746.

750 Sato, M. (1978) Oxygen fugacity of Basaltic Magmas and the Role of Gas Forming Elements.
751 *Geophysical Research Letters*, 5, 447–449.

752 Schreyeck, L., Wlosik, A., and Fuzellier, H. (2001) Influence of the synthesis route on $MgAl_2O_4$ spinel
753 properties. *Journal of Materials Chemistry*, 11, 483–486.

754 Sheldrick, G.M. (1997) Shelx-97-a program for crystal structure refinement. Institut für Anorganische
755 Chemie, University of Gottingen, Germany.

756 Wadhwa, M. (2008). Redox Conditions on Small Bodies, the Moon and Mars. *Reviews in Mineralogy*
757 *and Geochemistry*, 68(1), 493 LP-510.

758 Waychunas, G.A., Brown, G.E., and Apter, M.J. (1983) X-ray K-edge absorption spectra of Fe
759 minerals and model compounds: Near edge structure. *Physics and Chemistry of Minerals*, 10, 1–9.

760 Westre, T.E., Kennepohl, P., DeWitt, J.G., Hedman, B., Hodgson, K.O., and Solomon, E.I. (1997) A
761 multiplet analysis of Fe K-edge 1s - 3d pre-Edge features of iron complexes. *Journal of the American*
762 *Chemical Society*, 119, 6297–6314.

763 Wickham, D.G. (1969) The Chemical Composition of Spinel in the System $\text{Fe}_3\text{O}_4\text{-Mn}_3\text{O}_4$. *Journal of*
764 *Nuclear Inorganic Chemistry*, 31, 313–320.

765 Wijbrans, C.H., Klemme, S., Berndt, J., and Vollmer, C. (2015) Experimental determination of trace
766 element partition coefficients between spinel and silicate melt: the influence of chemical
767 composition and oxygen fugacity. *Contributions to Mineralogy and Petrology*, 169.

768 Wilke, M., Farges, F., Petit, P.-E., Brown, G.E., and Martin, F. (2001) Oxidation state and coordination
769 of Fe in minerals : An Fe K- XANES spectroscopic study. *American Mineralogist*, 86, 714–730.

770 Wilson, A.J.C., and Prince, E. (1999) International tables for X-ray crystallography, Volume C:
771 Mathematical, physical and chemical tables, 2nd ed. Kluwer Academic, Dordrecht, NL.

772 Wojdyr, M. (2010) Fityk: A general-purpose peak fitting program. *Journal of Applied Crystallography*,
773 43, 1126–1128.

774 Yamanaka, T., & Nakahira, M. (1973). Dependence of the cation distribution in manganese ferrite,
775 MnFe_2O_4 , on temperature and oxidation. *Mineralogical Journal*, 7(2), 202-220.

776 Yang, A.Y.A., Harris, V.G.G., Calvin, S., Zuo, X.Z.X., and Vittoria, C. (2004) Extended X-ray absorption
777 fine structure analysis of cation distribution in MnFe_2O_4 single crystal films and artificial ferrite
778 structures. *IEEE Transactions on Magnetics*, 40, 2802–2804.

779 Zhang, Z.J., Wang, Z.L., Chakoumakos, B.C., and Yin, J.S. (1998) Temperature Dependence of Cation
780 Distribution and Oxidation State in Magnetic Mn–Fe Ferrite Nanocrystals. *Journal of the American*
781 *Chemical Society*, 120, 1800–1804.

782 TABLE 1: Details pertaining to the X-ray single-crystal structure refinements of the galaxite and jacobsite samples.

| | GaAC | Ga93 | Ga90 | Ga60 | JcAC | Jc93 | Jc90 | 783 |
|---|--------------------------------------|--------------------------------------|--------------------------------------|--------------------------------------|--------------------------------------|--------------------------------------|--------------------------------------|-----|
| Crystal size (μm^3) | 200 x 170 x 100 | 190 x 160 x 90 | 220 x 180 x 150 | 250 x 180 x 120 | 260 x 170 x 110 | 270 x 200 x 130 | 200 x 120 x 90 | |
| Radiation, detector type | MoK α , CCD | MoK α , CCD | MoK α , CCD | MoK α , CCD | MoK α , CCD | MoK α , CCD | MoK α , CCD | |
| Scan type, width ($^\circ$), time/frame (s) | ω , 1, 10 | ω , 1, 10 | ω , 1, 10 | ω , 1, 10 | ω , 1, 10 | ω , 1, 10 | ω , 1, 10 | 784 |
| Temperature (K), Pressure (bar) | 293, 1 | 293, 1 | 293, 1 | 293, 1 | 293, 1 | 293, 1 | 293, 1 | |
| Reference chemical formula, Z | MnAl ₂ O ₄ , 8 | MnAl ₂ O ₄ , 8 | MnAl ₂ O ₄ , 8 | MnAl ₂ O ₄ , 8 | MnFe ₂ O ₄ , 8 | MnFe ₂ O ₄ , 8 | MnFe ₂ O ₄ , 8 | |
| Space group | <i>Fd-3m</i> | <i>Fd-3m</i> | <i>Fd-3m</i> | <i>Fd-3m</i> | <i>Fd-3m</i> | <i>Fd-3m</i> | <i>Fd-3m</i> | 785 |
| <i>a</i> (\AA) | 8.3541(2) | 8.3610(3) | 8.2210(16) | 8.3469(2) | 8.4957(3) | 8.4679(2) | 8.5415(8) | |
| θ_{max} ($^\circ$) | 35.57 | 35.54 | 35.45 | 35.61 | 35.85 | 35.98 | 35.62 | |
| | $-12 \leq h \leq 12$ | $-12 \leq h \leq 12$ | $-11 \leq h \leq 11$ | $-13 \leq h \leq 13$ | $-13 \leq h \leq 13$ | $-13 \leq h \leq 14$ | $-11 \leq h \leq 11$ | |
| | $-12 \leq k \leq 12$ | $-13 \leq k \leq 13$ | $-13 \leq k \leq 13$ | $-13 \leq k \leq 13$ | $-13 \leq k \leq 13$ | $-11 \leq k \leq 10$ | $-13 \leq k \leq 13$ | 786 |
| | $-13 \leq l \leq 13$ | $-11 \leq l \leq 11$ | $-11 \leq l \leq 11$ | $-11 \leq l \leq 11$ | $-11 \leq l \leq 11$ | $-13 \leq l \leq 13$ | $-13 \leq l \leq 13$ | |
| No. collected reflections | 3652 | 3723 | 3456 | 3711 | 3852 | 3542 | 3357 | |
| No. unique reflections | 85 | 87 | 82 | 85 | 90 | 88 | 79 | |
| No. unique refl. with $F_o > 4\sigma(F_o)$ | 82 | 81 | 82 | 79 | 88 | 86 | 75 | 787 |
| No. refined parameters | 10 | 10 | 10 | 10 | 10 | 10 | 10 | |
| Extinction parameter | 0.0010(6) | 0.0039(6) | 0.001(1) | 0.0013(5) | 0.014(1) | 0.0030(5) | 0.0075(8) | |
| R_{int} | 0.0441 | 0.0404 | 0.0529 | 0.0288 | 0.0453 | 0.0667 | 0.0779 | 788 |
| $R_1(F)$ with $F_o > 4\sigma(F_o)$ | 0.0183 | 0.0146 | 0.0429 | 0.0170 | 0.0144 | 0.0171 | 0.0317 | |
| $wR_2(F^2)$ | 0.0398 | 0.0335 | 0.0907 | 0.0331 | 0.0343 | 0.0371 | 0.0366 | |
| GooF | 1.774 | 1.523 | 3.583 | 1.550 | 1.749 | 1.719 | 1.595 | |
| Residual $\rho_{\text{max}}/\rho_{\text{min}}$ ($e^-/\text{\AA}^3$) | +0.23/-0.28 | +0.33/-0.28 | +0.95/-0.80 | +0.26/-0.26 | +0.36/-0.28 | +0.36/-0.53 | +0.96/-0.59 | 789 |
| $T(8a)$, $x=1/8$ | | | | | | | | |
| U_{11} (\AA^2) | 0.0130(3) | 0.0120(2) | 0.0110(6) | 0.0119(2) | 0.0074(3) | 0.0060(3) | 0.0072(4) | |
| $M(16d)$, $x=1/2$ | | | | | | | | 790 |
| U_{11} (\AA^2) | 0.0134(2) | 0.0121(2) | 0.0128(6) | 0.0124(2) | 0.0071(2) | 0.0059(2) | 0.0069(3) | |
| U_{12} (\AA^2) | -0.0013(1) | -0.0012(1) | 0.0001(3) | -0.0011(1) | -0.00101(8) | -0.00095(9) | -0.0007(2) | |
| $O(32e)$ | | | | | | | | |
| x (u) | 0.26439(15) | 0.26433(13) | 0.2646(3) | 0.26432(13) | 0.26181(14) | 0.26151(15) | 0.2607(2) | 791 |
| U_{11} (\AA^2) | 0.0254(6) | 0.0250(5) | 0.0154(10) | 0.0251(5) | 0.0136(6) | 0.0110(6) | 0.0142(8) | |
| U_{12} (\AA^2) | -0.0030(4) | -0.0033(4) | 0.0001(7) | -0.0031(4) | -0.0009(3) | 0.0001(4) | -0.0001(8) | |
| $T-O$ (\AA) | 2.017(2) | 2.018(2) | 1.987(4) | 2.014(2) | 2.013(2) | 2.002(2) | 2.008(3) | 792 |
| $M-O$ (\AA) | 1.9757(11) | 1.9777(9) | 1.943(2) | 1.9745(9) | 2.029(1) | 2.024(1) | 2.048(2) | |
| <p>Note: origin fixed at $\bar{3}m$; $R_{\text{int}} = \sum F_o^2 - F_o^2(\text{mean}) / \sum [F_{\text{obs}}^2]$; $R_1(F) = \sum (F_o - F_c) / \sum F_o$; $wR_2(F^2) = [\sum [w(F_o^2 - F_c^2)^2] / \sum [w(F_o^2)^2]]^{0.5}$; s.o.f. are given in Table 3, as refined atomic fraction and as electron content per site Σe^-. The anisotropic displacement factor exponent takes the form: $-2\pi^2[(ha^*)^2 U_{11} + \dots + 2hka^*b^* U_{12} + \dots + 2k1b^*c^* U_{23}]$.</p> | | | | | | | | 793 |

794 TABLE 2: Averaged compositions and element totals of jacobsite and galaxite samples determined by
 795 electron microprobe¹

796

| | Al | Mn | Fe | O | Total ² | Formula based on 4 Oxygen | Est Mn valence |
|------------------------------|-----------|------------|------------|-----------|--------------------|---|----------------|
| GaAC | 15.57(71) | 51.86(96) | bd | 32.83(38) | 100.29(37) | Mn _{1.84} Al _{1.12} O ₄ | 2.52 |
| Ga93 | 15.76(37) | 52.12(44) | bd | 33.24(54) | 100.96(38) | Mn _{1.83} Al _{1.12} O ₄ | 2.54 |
| Ga90 | 13.61(96) | 54.77(127) | bd | 32.01(47) | 100.33(31) | Mn _{1.99} Al _{1.01} O ₄ | 2.50 |
| Ga60 | 30.95(30) | 31.25(25) | bd | 36.65(22) | 103.21(47) | Mn _{0.99} Al _{2.00} O ₄ | 2.02 |
| Galaxite³ | 31.21 | 31.77 | bd | 37.01 | - | MnAl ₂ O ₄ | |
| JcAC | bd | 3.04(55) | 66.93(56) | 29.30(16) | 99.27(25) | Mn _{0.12} Fe _{2.62} O ₄ | |
| Jc93 | 0.78(21) | 19.68(84) | 51.29(104) | 27.07(14) | 98.83(16) | Mn _{0.85} Al _{0.07} Fe _{2.17} O ₄ | |
| Jc90 | 0.21(8) | 32.14(51) | 39.20(80) | 27.31(49) | 98.86(93) | Mn _{1.37} Al _{0.02} Fe _{1.64} O ₄ | |
| Jacobsite³ | bd | 23.82 | 48.43 | 27.75 | - | MnFe ₂ O ₄ | |

797 ¹Figures in parentheses are the standard deviations on the last significant figure of the average value,
 798 including element totals.

799 ²Average of the element totals for all analyses

800 ³Compositions of the ideal end member

801

802 TABLE 3: SC-XRD refinements for galaxite group data, and refinement which includes cation distribution based on modelling of bond lengths. Δ (Σe^- p.f.u.) %
 803 is defined as the difference of the total e^- number between the structural refinement and the final refinement based on bond length modelling.

| Group | Crystal formula based on the structure refinement, with site distributions | General formula based on the structure refinement | Electron distribution per site and total e^- number based on the structure refinement | Final refinement based on bond length modelling | Δ (Σe^- p.f.u.) % | Est. Average Mn valence |
|-------|--|---|---|--|-----------------------------------|-------------------------|
| GaAC | $T[Mn_{0.846}Al_{0.154}]^M[Al_{0.542}Mn_{0.458}]_2O_4$ | $Mn_{1.762(36)}Al_{1.238(36)}O_4$ | Σe^- p.f.u. = $Mn(44.1(9) e^-) + Al(16.1(4) e^-) = 60.2(13) e^-$ | $T[Mn_{0.846}^{2+}Al_{0.154}^{3+}]^M[Al_{0.542}^{3+}Mn_{0.075}^{2+}Mn_{0.383}^{3+}]_2O_4$ | 0.06 | 2.43 |
| Ga93 | $T[Mn_{0.835}Al_{0.165}]^M[Al_{0.545}Mn_{0.455}]_2O_4$ | $Mn_{1.745(28)}Al_{1.255(28)}O_4$ | Σe^- p.f.u. = $Mn(43.6(6) e^-) + Al(16.3(3) e^-) = 59.9(9) e^-$ | $T[Mn_{0.835}^{2+}Al_{0.165}^{3+}]^M[Al_{0.545}^{3+}Mn_{0.08}^{2+}Mn_{0.375}^{3+}]_2O_4$ | 0.04 | 2.43 |
| Ga60 | $T[Mn_{0.82}Al_{0.18}]^M[Al_{0.587}Mn_{0.413}]_2O_4$ | $Mn_{1.646(26)}Al_{1.354(26)}O_4$ | Σe^- p.f.u. = $Mn(41.1(7) e^-) + Al(17.6(3) e^-) = 58.7(10) e^-$ | $T[Mn_{0.820}^{2+}Al_{0.180}^{3+}]^M[Al_{0.587}^{3+}Mn_{0.095}^{2+}Mn_{0.318}^{3+}]_2O_4$ | 0.05 | 2.39 |
| Ga90 | $T[Mn_{0.98}Al_{0.02}]^M[Al_{0.79}Mn_{0.21}]_2O_4$ | $Mn_{1.34(7)}Al_{1.60(7)}O_4$ | Σe^- p.f.u. = $Mn(33.5(17) e^-) + Al(20.8(9) e^-) = 54.3(25) e^-$ | $T[Mn_{0.800}^{2+}Mn_{0.180}^{3+}Al_{0.020}^{3+}]^M[Al_{0.790}^{3+}Mn_{0.100}^{2+}Mn_{0.110}^{3+}]_2O_4$ | 1.50 | 2.18 |
| JaAC | $T[Fe_{0.936(12)}]_M[Fe_{0.926(11)}]_2O_4$ | $^{(T+M)}Fe_{2.788(34)}O_4$ | Σe^- p.f.u. = 72.5(8) e^- | | | |
| Ja93 | $T[Fe_{0.921(11)}]_M[Fe_{0.884(10)}]_2O_4$ | $^{(T+M)}Fe_{2.689(31)}O_4$ | Σe^- p.f.u. = 69.9(8) e^- | | | |
| Ja90 | $T[Fe_{0.909(11)}]_M[Fe_{0.937(10)}]_2O_4$ | $^{(T+M)}Fe_{2.783(31)}O_4$ | Σe^- p.f.u. = 72.4(7) e^- | | | |

804

805 TABLE 4: Mn K-edge pre-peak data for galaxite and jacobsite samples, and Fe K-edge data from jacobsite spectra

| Sample | Mn K edge | | | Fe K edge | | |
|--------|-----------|---------------|-------|---------------|-------|----------------------|
| | % M | Centroid (eV) | Area | Centroid (eV) | Area | Est. average valence |
| GaAC | 52 | 6539.04 | 0.089 | | | |
| Ga93 | 52 | 6539.04 | 0.092 | | | |
| Ga90 | 50 | 6539.05 | 0.108 | | | |
| Ga60 | 31 | 6539.02 | 0.216 | | | |
| JcAC | | 6539.87 | 0.230 | 7113.14 | 0.090 | 2.98 |
| Jc93 | | 6539.28 | 0.210 | 7112.81 | 0.060 | 2.74 |
| Jc90 | | 6539.24 | 0.190 | 7112.73 | 0.068 | 2.70 |

806 TABLE 5: Effective cation-oxygen bond length for oxide spinels (after Lavina et al. 2002)

| | Al | Mn ²⁺ | Mn ³⁺ | Mn ⁴⁺ | Fe ²⁺ | Fe ³⁺ | Vacancies |
|---------------------|-------|------------------|------------------|------------------|------------------|------------------|-----------|
| T-O bond length (Å) | 1.774 | 2.04 | 1.880 | 1.770 | 1.996 | 1.891 | 2.000 |
| M-O bond length (Å) | 1.909 | 2.191 | 2.030 | 1.910 | 2.138 | 2.020 | 2.110 |

807

808

809 FIG. 1: Normalized Mn K-edge XANES spectra for galaxite samples AC, 93, 90 and 60 (offset vertically
810 for clarity.

811

812 FIG. 2: **Top**: Fe K-edge XANES spectra of jacobsite spinel synthesized with: 93%, 90% CO₂ and no gas
813 flow. **Bottom** Mn K-edge XANES spectra of jacobsite spinel synthesized with: 93% CO₂, 90% CO₂ and
814 no gas flow

815